INVESTIGATIONS OF LOX/CH4 FLAMES AT VERY LOW MIXTURE RATIO AND HIGH PRESSURE IN ROCKET ENGINE OPERATING CONDITIONS

Valentin Lechner, Christopher Betrancourt, Sebastien Ducruix, Philippe Scouflaire, Nicolas Fdida, Lucien Vingert, Marie Théron, Alexandre Barata, Marie Robcis

INVESTIGATIONS OF LOX/CH_4 FLAMES AT VERY LOW MIXTURE RATIO AND HIGH PRESSURE IN ROCKET ENGINE OPERATING CONDITIONS

V. Lechner[1, 2], C. Betrancourt[2], S. Ducruix[2], P. Scouflaire[2], N. Fdida[3], L. Vingert[3], M. Theron[1], A. Barata[4], M. Robcis[4]

[1]CNES, Launcher Directorate, Paris, France
[2]EM2C laboratory, CNRS, CentraleSupélec, Paris-Saclay University, Gif-Sur-Yvette, France
[3]ONERA, The French Aerospace Lab, Palaiseau, France
[4]ArianeGroup SAS, Vernon, France

KEYWORDS: Liquid Rocket Engine, oxygen/methane, transcritical combustion, surface thermometry, soot measurements

ABSTRACT:

Experiments are conducted by Lab. EM2C, ONERA, CNES, and ArianeGroup on the cryotechnic test bench MASCOTTE to investigate conditions like those encountered on the gas generator of liquid rocket engines fed with methane and oxygen: low mixture ratio (0.3) and high pressure (26 to 60 bar). Propellants are injected through a single coaxial injection element with or without recess and in subcritical or transcritical conditions. Coupled high-speed flame visualization with backlighting imaging of the liquid jets, dynamic surface thermometry by Laser Induced Phosphorescence, and soot measurements by laser extinction are implemented simultaneously to characterize the flame and its effects.

1. Introduction

The rising diversity of Liquid Rocket Engines (LRE): Prometheus (ESA/ArianeGroup), Raptor (SpaceX), Archimedes (Rocket Lab), BE-4 (Blue Origin), TQ (LandSpace), Aeon 1 (Relativity Space) … proves a growing interest in liquid oxygen (LOX) and liquid methane (LCH4) as propellants combination. Methane has many advantages, although it offers a lower specific impulse (ISP) than hydrogen. Its liquefaction temperature is close to that of oxygen, facilitating its storage and handling, and its density is six times greater than that of hydrogen, making it possible to use smaller tanks. Methane is a standard fuel used in many applications, can be extracted from natural gas, and its production is well managed. However, the combustion of methane and pure oxygen at high pressure remains poorly understood, particularly under the conditions encountered in the gas generator of LRE.

Understanding the different heat transfer mode contributions is mandatory for the development of a reusable rocket engine, which life cycle highly depends on the accuracy of wall temperature prediction. Moreover, different flame topologies can be triggered by wall temperatures [1] and retrieved by numerical simulations thanks to precise boundary conditions [2]. Thus, several groups have measured wall heat fluxes in subscale experiments and showed the influence of the injection element design [3] and arrangement [4], or chamber pressure [5, 6]. More accurate and time-resolved measurements are still necessary in representative rocket engine operating conditions.

Methane being carbon-based and gas generator usually working in fuel-rich conditions, soot particles are expected. Soot is a primary carbonaceous particle resulting from the incomplete combustion of hydrocarbons. Some benefits can be found in the main thrust chamber by the induced protective carbon layer deposing on the wall, thus protecting them from high heat fluxes [7]. However, because clogging and damage to the turbine can append [8–10], soot are of great concern in the gas generator, not to mention a significant health and environmental problem. Soot need thus to be characterized to enable a thorough evaluation of their potential impact on engine performance and life duration.

Imaging the flame allows a direct two dimensions comparison with numerical simulations [11] and is frequently implemented in subscale rocket engine experiments. Many studies have thus shown a strong dependence of the flame shape on the injection element geometry and the injection conditions. For example, a better stabilization of the flame is found with a recess in the injection element, enhancing oxygen atomization, mixing, and so the flame opening angle [12–14]. However, there are few flame visualizations in conditions where both methane and oxygen are in liquid or transcritical states [15].

These challenges are tackled within the Lab. EM2C/ONERA/CNES/ArianeGroup R&D consortium through experimental investigations held at the MASCOTTE test bench [16], located at

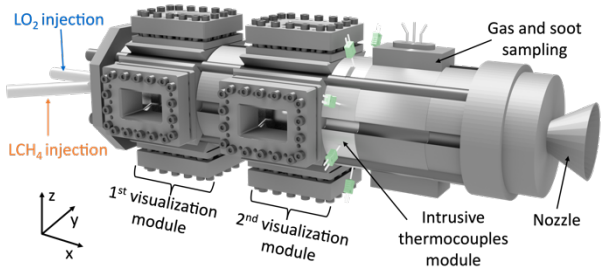

Figure 1. Schematic representation of the BHP combustion chamber.

ONERA Palaiseau center. The BHP combustion chamber is equipped with a single coaxial injection element. Advanced diagnostics are implemented simultaneously to understand the behavior of LOX/CH_4 cryogenic flames at a low mixture ratio (MR = 0.3) and when LOX and CH_4 are injected in either subcritical or transcritical states (26, 48, and 60 bar) to mimic engine throttling.

High-speed backlighting imaging, OH* and CH* chemiluminescence detection are coupled and synchronized to observe the structure of the liquid jets and the flame.

Laser Induced Phosphorescence (LIP) thermometry [17] is implemented to track simultaneously the temperature of five surfaces of the combustion chamber during hot firing tests. LIP relies on applying a thermographic phosphor coating on surfaces of interest. A phosphorescence signal is emitted under laser irradiation which is temporally and spectrally temperature-dependent. These properties are used to determine an unknown temperature through an appropriate calibration. A dedicated method developed by Lab. EM2C, the FSF method [18], allows single-shot measurements in an 800 K temperature range with a unique set of experimental acquisition parameters.

Laser extinction is implemented to determine the soot volume fraction in the burnt gases downstream of the flame. This optical diagnostic relies on measuring the attenuation of an incident light by the absorbing medium [19].

2. EXPERIMENTAL SETUP

2.1. MASCOTTE cryotechnic test bench and operating conditions

Experiments are conducted on the high-pressure combustion chamber (BHP) of the cryotechnic test bench MASCOTTE operated by ONERA [16]. As seen in Fig. 1, it is composed of different modules of 50×50 mm^2 section. For the first time, two visualization modules are used simultaneously for optical accesses from the injection exit and downstream of the flame. Three silica windows (Corning 7980), providing a 40×75 mm^2 view, are mounted on the first module. The two on the side are used for high-speed visualization of the flame and liquid jets, whereas the third one, at the bottom, is used for phosphor thermometry. Two silica windows are mounted on the side of the second module for LIP and laser extinction measurements. A J-type thermocouple is inserted in the bottom blind window made of stainless steel to measure its surface temperature (see Fig. 3).

The 2nd visualization module is followed by a module including seven ungrounded sheathed thermocouples of 2 mm diameter. Their names, type, and radial positions are indicated in Fig. 3. Gas and soot are sampled downstream of the flame with a special intrusive probe to analyze the composition of burnt gases and the type and morphology of soot [20]. This is, however, outside the scope of this paper.

Methane and oxygen are injected into the combustion chamber through the injector head, and a single classical liquid rocket engine sheared injection element. A central tube (LOX post) supplies the oxygen, and the outer tube supplies the methane. Two versions are used, with (WR) or without (NR) recess of the LOX post. Calibration parts are added upstream of the injector outlet to reproduce the pressure drops encountered by the propellants in the engine.

Operating conditions are gathered in Tab. 1. The mixture ratio, defined as $\mathrm{MR} = \dot{m}_{O_2}/\dot{m}_{CH_4}$, is kept constant at 0.3. Oxygen and methane thermodynamic states are defined from the value of their critical points $P_c(O_2) =$ 50.4 bar, $T_c(O_2) = 154$ K, and $P_c(CH_4) = 46.0$ bar, $T_c(CH_4) = 190$ K. The injection temperatures are kept constant for all operating points and always below both critical temperatures. Therefore, the reduced pressure $\pi_r = P_{chamber}/P_c$, characterizes subcritical ($\pi_r < 1$) and transcritical ($\pi_r > 1$) states. Three chamber pressures are targeted to reach different combinations of thermodynamic conditions. Chamber pressure is measured by a Kulite sensor in the first visualization module, located in the blind window on the top, next to the H_2/O_2 ignition torch.

Table 1. Operating conditions.

Name		P26	P48	P60
Pressure (bar)		26	48	60
MR (-)		0.3	0.3	0.3
T_{inj} (K)	O_2	110	110	110
	CH_4	140	140	140
π_r (-)	O_2	0.52	0.95	1.19
	CH_4	0.56	1.04	1.30
Thermo. state	O_2	sub.	sub.	trans.
	CH_4	sub.	trans.	trans.

Six operating points are thus defined with three targeted pressures and two injection element

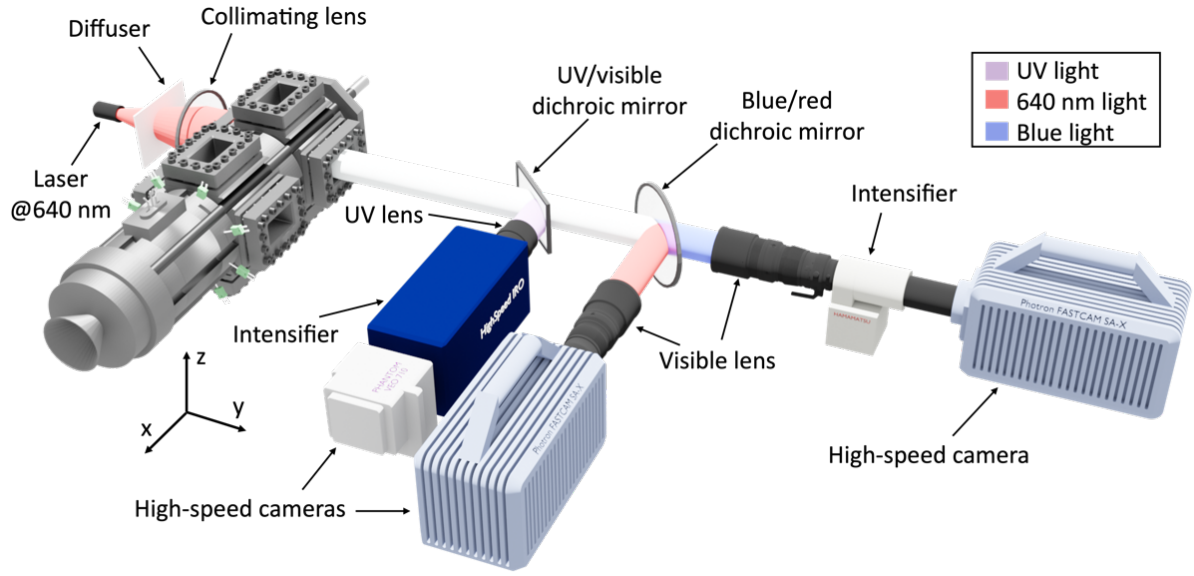

Figure 2. Schematic of the high-speed imaging setup.

geometries. They are designated as the combination of the injection element geometry (WR or NR) and chamber pressure (P26, P48, or P60).

2.2. Optical diagnostics

2.2.1. High-speed imaging

Backlighting imaging, OH*, and CH* chemiluminescence detection are implemented simultaneously and synchronized. Fig. 2 shows this imaging setup on the BHP combustion chamber.

Some chemical reactions produce radical species in excited states during combustion, emitting a photon at a characteristic wavelength during spontaneous decay. Chemiluminescence is this spontaneous light emission which thus allows the identification of the flame front. OH* and CH* radicals are widely used to characterize oxygen/methane combustion [14, 21, 22] and emit light at central wavelengths of 308 nm and 431 nm, respectively.

Intensifiers coupled with high-speed 12-bit monochrome cameras are used to detect OH* and CH* emissions (LaVision HighSpeed IRO and Phantom VEO 710 for OH*, Hamamatsu and Photron SA-X2 for CH*). A 100 mm UV objective (CERCO) opened at f/8 equipped with a filter centered at 310 nm with 10 nm half-width is used for OH* emission detection. A 200 mm visible objective (Nikkor) opened at f/8 equipped with a filter centered at 430 nm with 10 nm half-width is used for CH*. The intensifiers gain and the cameras exposure time are kept constants for all operating points. The gate-opening time of intensifiers sets, however, the effective exposure. They are adapted through the campaign to maximize the signal-to-noise ratio. Both exposure times are synchronized and vary from 400 to 1200 ns for OH* and 1000 to 4500 ns for CH*. These values allow obtaining satisfactory instantaneous images of the flame. A higher exposure time is required for CH* emission detection, so instantaneous CH* images are more time-averaged than OH* images.

Backlighting imaging consists of a pulsed light source placed in front of the flame and the liquid jets [23]. A camera detects the transmitted light on the opposite side. Dense liquid areas transmit less the incident light than gases of lower densities. Liquid structures thus appear in black on the detector. The light source is a pulsed laser (Cavitar Cavilux Smart 400 W) emitting at 640 ± 10 nm. A diffuser and a lens (350 mm focal length) are used to illuminate the whole window. The transmitted light is detected with a 12-bit monochrome high-speed camera (Photron SA-X2) equipped with a 200 mm visible objective (Nikkor) opened at f/8. The exposure time is fixed by the laser exposition, which freezes the flow and varies from 40 to 60 ns. The camera exposure time is set to 5 µs so that the flame emission may be visible and quite similar to CH* images.

The three cameras are focused on the same field of view, with similar resolutions, thanks to dichroic mirrors. The first one separates the UV and visible light, and the second one reflects light above 660 nm. The sensors are reduced to 496 × 896 pixels to fit the BHP window size and enable fast acquisition leading to a resolution of 11.6 mm/pixel for backlighting and 10.5 mm/pixel for OH* and CH* emission detection.

The three cameras are synchronized to record the entire combustion process from ignition to extinction with a 1 kHz frame rate or record a 3 s

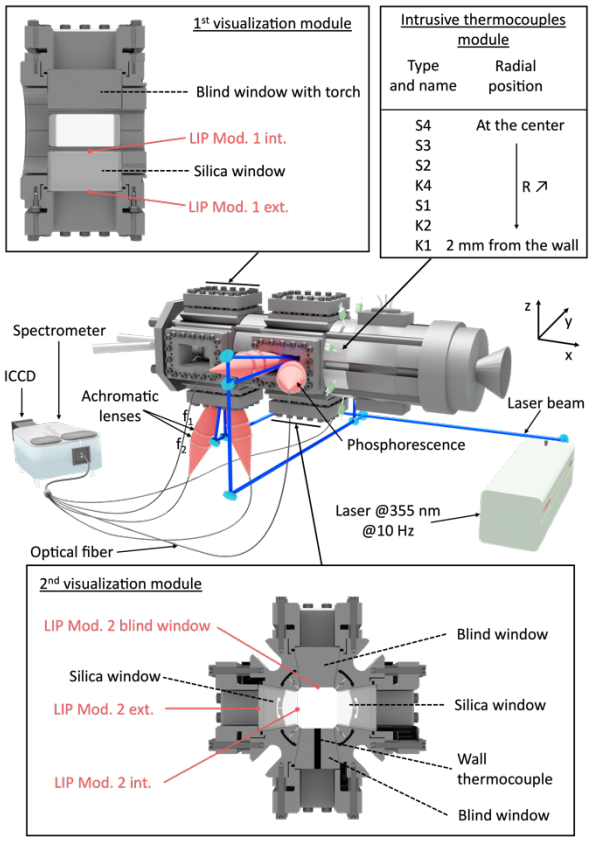

Figure 3. Schematic of the phosphor thermometry setup.

film during the stabilized time-step, starting at t = 40 s with a 15 kHz frame rate. About 52 000 images are captured in both situations for each device. For chemiluminescence images, summing up the intensity of each pixel allows tracking the overall intensity of the flame as a function of time to detect the different stages during the run.

2.2.2.Phosphor thermometry

The coating is obtained by mixing $Mg_{3.5}FGeO_5$:Mn phosphor powder (Phosphor Technology, EQD25/NU1) with a commercial binder (ZYP Coatings, HPC Binder) and water. This mixture is coated with an airbrush with ten layers. As seen in Fig. 3, two measurements are performed in the first visualization module and three in the second module. In the first and second modules, silica windows are coated on the internal and external sides. The fifth coating is applied on a blind window in the second module. Each measurement is performed in the middle of the windows.

The coated surfaces are excited at 355 nm using the 3rd harmonic of a pulsed Nd:YAG laser (Continuum, Surelite SL II-10) triggered at 10 Hz. The laser beam is distributed to the five locations with beamsplitters leading to a 64 mJ.cm^{-2} fluence at each measurement site.

Telescopes composed of two-inch achromatic lenses ($f_1 = 150$ mm and $f_2 = 100$ mm) are used to collect phosphorescence signals. The light is

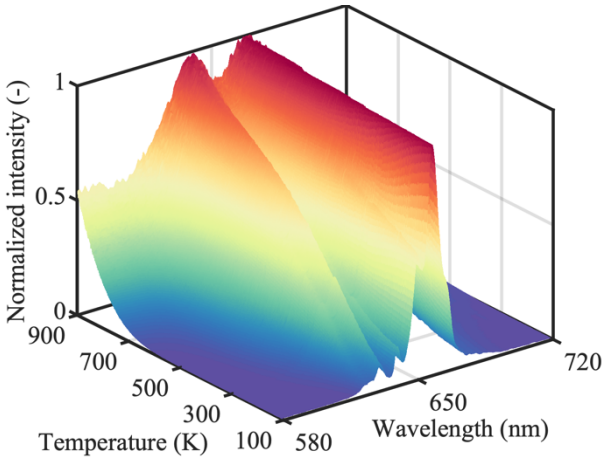

Figure 4. Phosphorescence spectra database at 64 mJ.cm^{-2}.

then focused on a 200 µm multimode optical fiber (CeramOptec, customized). All fibers are joined in a bundle and are aligned vertically, leading to the entrance slit of a spectrometer (Princeton Instrument, Spectra Pro 500i, $f = 500$ mm, grating of 150 grooves mm^{-1}). Phosphorescence signals are imaged at 10 Hz with the spectrometer coupled with an intensified CCD camera (Princeton Instrument, Pi-Max, 512 × 512 pixel^2) covering a spectral range of 160 nm centered at $\lambda = 650$ nm. The exposure time is set to 30 µs. Each single-shot spectrum is corrected from the dark current and smoothed with a 3-order Savitzky-Golay filter.

LIP calibration was carried out previously in Lab. EM2C by building databases of phosphorescence spectra at each kelvin from 100 K to 900 K, and laser fluences from 11 to 106 mJ·cm^{-2} at atmospheric pressure. Fig. 4 shows an example of a database at 64 mJ.cm^{-2}. The Full Spectrum Fitting method (FSF method) [18] is applied to determine the temperature from the single-shots acquired. A least mean square algorithm is used to find the best agreement between each measured spectrum and one from the database. All the databases at different laser fluences are checked with this procedure leading to the final targeted temperature. This post-processing approach allows being nearly independent of the excitation energy, which can be lower than the calibration one in this high absorbing environment [18].

In this work, temperatures are presented in the normalized form θ.

2.2.3.Laser extinction

Soot absorbs and scatters light broadband UV to IR. From the Beer-Lamber law, the transmitted light through a homogeneous optically thin medium is:

$$I = I_0 e^{-K_\lambda^{ext} L}, \qquad \text{Eq. 1}$$

with I_0 the incident light intensity at wavelength λ

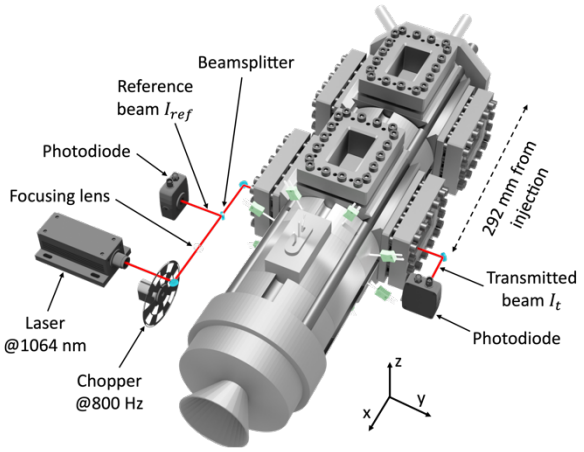

Figure 5. Schematic of the laser extinction setup.

before crossing the medium, L the length of the medium and K_λ^{ext} the extinction coefficient. Extinction is defined as the sum of absorption and scattering by the particles:

$$K_\lambda^{ext} = K_\lambda^{abs} + K_\lambda^{sca}. \qquad \text{Eq. 2}$$

No molecular absorption is expected at 1064 nm. Within the Rayleigh limit, it is common to neglect scattering, assuming that soot are small spherical particles $\left(\frac{\pi D_p}{\lambda} < 1\right)$. For most applications in sooting flames, the Rayleigh-Debye-Gans approximation is applied [24], giving the absorption coefficient of an aggregate from the absorption for the N_p individual particles:

$$K_\lambda^{abs} = N_p \cdot K_\lambda^{abs,p}. \qquad \text{Eq. 3}$$

The absorption coefficient is then given by the Rayleigh theory for isotropic spheres:

$$K_\lambda^{abs,p} = \pi^2 \frac{{D_p}^3}{\lambda} E(m_\lambda), \qquad \text{Eq. 4}$$

with D_p the primary particles diameter and $E(m_\lambda)$ the soot absorption function, which depends on their optical properties and maturity stage [25]. The soot volume fraction can finally be expressed as a function of the extinction coefficient:

$$f_v = N_p \frac{{D_p}^3}{6} = \frac{\lambda K_\lambda^{abs}}{6\pi E(m_\lambda)} = \frac{\lambda K_\lambda^{ext}}{6\pi E(m_\lambda)}. \qquad \text{Eq. 5}$$

K_λ^{ext} is determined experimentally from Eq. 1 by measuring I/I_0 to determine the soot volume fraction with Eq. 5.

Fig. 5 shows the laser extinction setup on the BHP combustion chamber. Measurements are performed in the second visualization module at $x = 292$ mm from the injection plate. The incident light is a continuous laser at $\lambda = 1064$ nm (Edmund MIL-III-1064-50mW) with a 1.5 mm diameter beam. A lens of 1 m focal length is used to collimate the laser beam and to correct the divergence of the laser. A mechanical chopper at 800 Hz is used to subtract any background signal. A first photodiode (Thorlabs, PDA50B2) measured the incident light I_{ref} before entering the combustion chamber to correct the laser intensity fluctuations. The transmitted light I_t is measured with the same photodiode model. Longpass filters with cut-on wavelengths at 1000 nm are mounted on the photodiodes. The large sensor size (19.6 mm^2) of the photodiodes prevents beam steering [26], occurring in thermal gradients and dense phases. Signals are acquired at 50 kHz with an acquisition card (NI-9239).

In this work, the soot volume fraction f_v is presented in a normalized form.

3. TEST SEQUENCE ANALYSIS

Fig. 6 shows the chronograph of a typical run at WRP48 operating point and the evolution of pressure, mixture ratio, gas and surface temperatures, soot volume fraction, OH* and CH* sum of intensities, and instantaneous images taken at different moments. The following paragraphs analyze the successive stages of the run thanks to these simultaneous diagnostics implemented.

3.1. Torch ignition

The main flame is ignited thanks to a secondary H_2/O_2 flame provided by the torch. A spark plug ignites a premix of gaseous hydrogen and oxygen, which is enabled during two seconds and starts at t = 25 s. At t = 26 s, this flame is recorded with high-speed cameras and detected by spontaneous emission of light by OH* radicals. As methane is not injected yet, no CH* radicals are produced. Raising the contrast allows the visualization of this flame. The bottom plot also shows a weak peak in the OH* sum of intensities. Besides, the presence of this gaseous flame results in a slight elevation of chamber pressure and gas temperature. Note that liquid oxygen is already injected into the combustion chamber but not completely vaporized and burnt. Filaments and individual droplets are indeed visible in the backlighting image. There is no increase in surface temperatures yet, but the slow acquisition of LIP measurements (10 Hz) may limit the recording of this event.

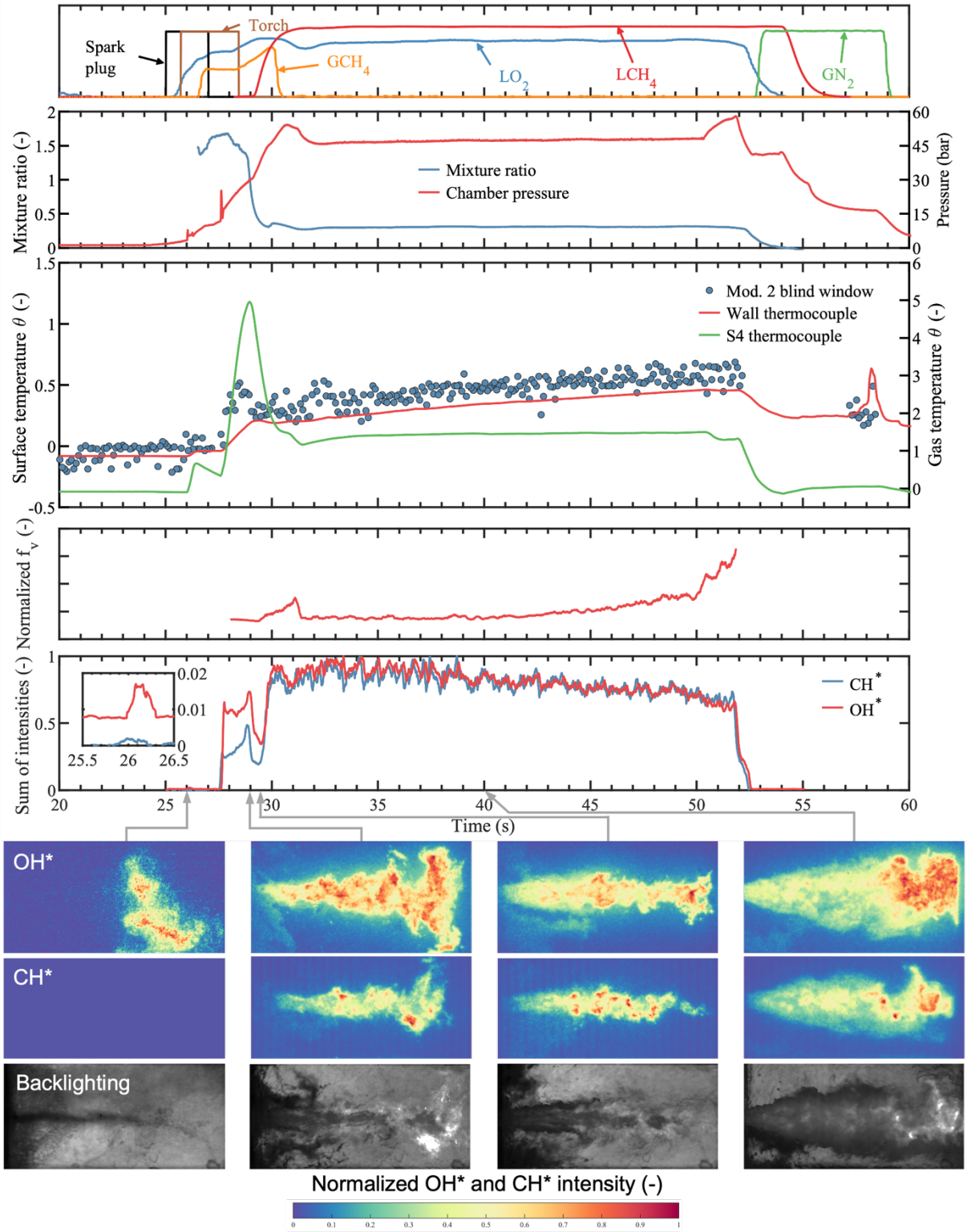

Figure 6. Typical run at WRP48 operating point. From top to bottom, evolution of: normalized mass flow rates, chamber pressure and mixture ratio, gas and surface temperatures, normalized soot volume fraction f_v, sums of OH and CH* intensities, and instantaneous OH*, CH* and backlighting images at different instants.*

3.2. LOX/GCH$_4$ flame

Gaseous methane starts being injected through the outer tube of the injection element one second after the opening of the H_2/O_2 torch. It ignites the LOX/GCH$_4$ flame at t = 27.5 s, as seen in the bottom plot's abrupt temperature rise and OH* and CH* intensities. There is also a pressure rise of 13 bar. In the gas phase, the mixture ratio is thus higher than targeted with liquid methane (but still below the stoechiometric value of 4) for almost four seconds, up to t = 29 s. During this period, oxygen is still in a subcritical state for all operating points. Due to the high velocity ratio between methane and liquid oxygen, liquid ligaments are broken away by shear effect before atomization, mixing,

and combustion with gaseous methane [27]. It results in a temperature peak broader and greater than the one during the torch ignition. It is well captured by phosphor thermometry. Typical instantaneous images of the flame are presented at t = 29 s, at maximum gas temperature, and just before the injection of liquid methane. Note that CH* and OH* images are slightly different due to their different exposure time values. CH* images are thus a bit more averaged in time than OH* images. A part of the flame emission is also captured by the backlighting camera. It is visible on the right part of the image and quite like the CH* one. OH* and CH* images show roughly the same properties: a bright flame covering the whole window with clear flame front demarcation and small spreading. It is unclear whether the flame closes at the window length or beyond. The entire surface of the flame is visible as methane is being injected into gas phase, and the intensity is relatively homogeneous except at the injection element exit. Here, a dense phase, appearing in blue in OH* and CH* images, black in the backlighting image, and probably condensed water, masks the flame's anchoring. For 27.5 s < t < 29 s, the light intensity continuously rises, reaching a level almost two times lower for CH* compared to OH*.

3.3. LCH_4 injection

Liquid methane starts being injected shortly after t = 29 s. It is followed by a decrease in gas and surface temperature resulting from the decrease in the mixture ratio. Up to t = 30.5 s, the pressure rises with the methane mass flow rate increase. The broad pressure peak corresponds to the injection of gaseous helium near silica windows to protect them from the temperature peak at ignition. The lower plot shows a sudden decrease of OH* and CH* intensities during the beginning of LCH_4 injection. The corresponding instantaneous images are presented at their lower intensities, at t = 29.5 s. One can see darker zones surrounding the flame near the injection on OH* and CH* images corresponding to liquid methane jet as seen on the backlighting image. The flame is shorter and tighter, so the apparent surface is smaller, explaining the lower sum of intensities. The intensities then rise again with the methane mass flow rate increase before reaching a plateau starting at t = 32 s.

3.4. LOX/LCH_4 targeted flame

The main LOX/LCH_4 is stabilized with the targeted mixture ratio and chamber pressure at t = 32 s and maintained for 18 s. The temperature of burnt gases almost reaches a steady state, whereas surfaces temperature continuously increases during the whole run up to t = 52 s. It should be noted that the BHP is an uncooled combustion chamber that functions like a heat sink, which explains the surface temperature increase. OH* and CH* reach the same level of intensity and show the same evolution. However, the intensity ratio between LOX/GCH_4 and LOX/LCH_4 flames is different for OH* and CH* emissions, indicating changes in the emission spectra. One can see a decrease of intensity as a function of time due to deposits on windows allowing less light to pass through them, degrading the quality of images. Besides, it has been observed for the laser extinction technique that the intensity I_0, recorded before and after each run decreases by 30 % after the run due to these deposits.

Typical instantaneous images taken during this stabilized time step, at t = 40 s, are presented. They show different properties compared to LOX/GCH_4 flames. The intensity is not homogenous: an intense zone is located downstream, whereas the intensity is lower on the left part of the window as liquid methane may mask the flame. This can be seen on the backlighting image: a wide liquid methane jet with wide-spreading, is hiding the liquid oxygen jet. A bright zone can be seen as well on the right. It corresponds to the flame emission, its shape matching the CH* image quite well. The flame front is thus less distinguishable than with gaseous methane. Anyway, the flame covers the whole window with wider spreading and may be longer. It has been identified indeed that the flame closes outside the window. Again, a dense condensed phase has been regularly observed recirculating around the conic flame near the injection and may be water. It was already observed in past studies [15] and often masks the flame anchoring. The intensity is thus lower in this zone, so it is challenging to discuss the flame anchoring on the injection element.

3.5. Flame extinction

Gaseous helium is injected near the windows for five seconds, starting at t = 50 s, rising the chamber pressure, and decreasing gas temperature. The oxygen mass flow rate slowly decreases from t = 52 s, leading to a lower mixture ratio, lower temperatures, and lower OH* and CH* intensities. Before reducing the methane mass flow rate, a gaseous nitrogen purge completely extinguishes the flame at t = 53 s. Pressure and temperatures finally strongly decrease with the flame extinction. The gaseous nitrogen purge is also used to prevent any detonation or backfire. For 53 s < t < 57 s, liquid methane is still injected but not burned. The lack of LIP measurements may be explained by the absorption or scattering of the phosphorescence signal by these dense structures.

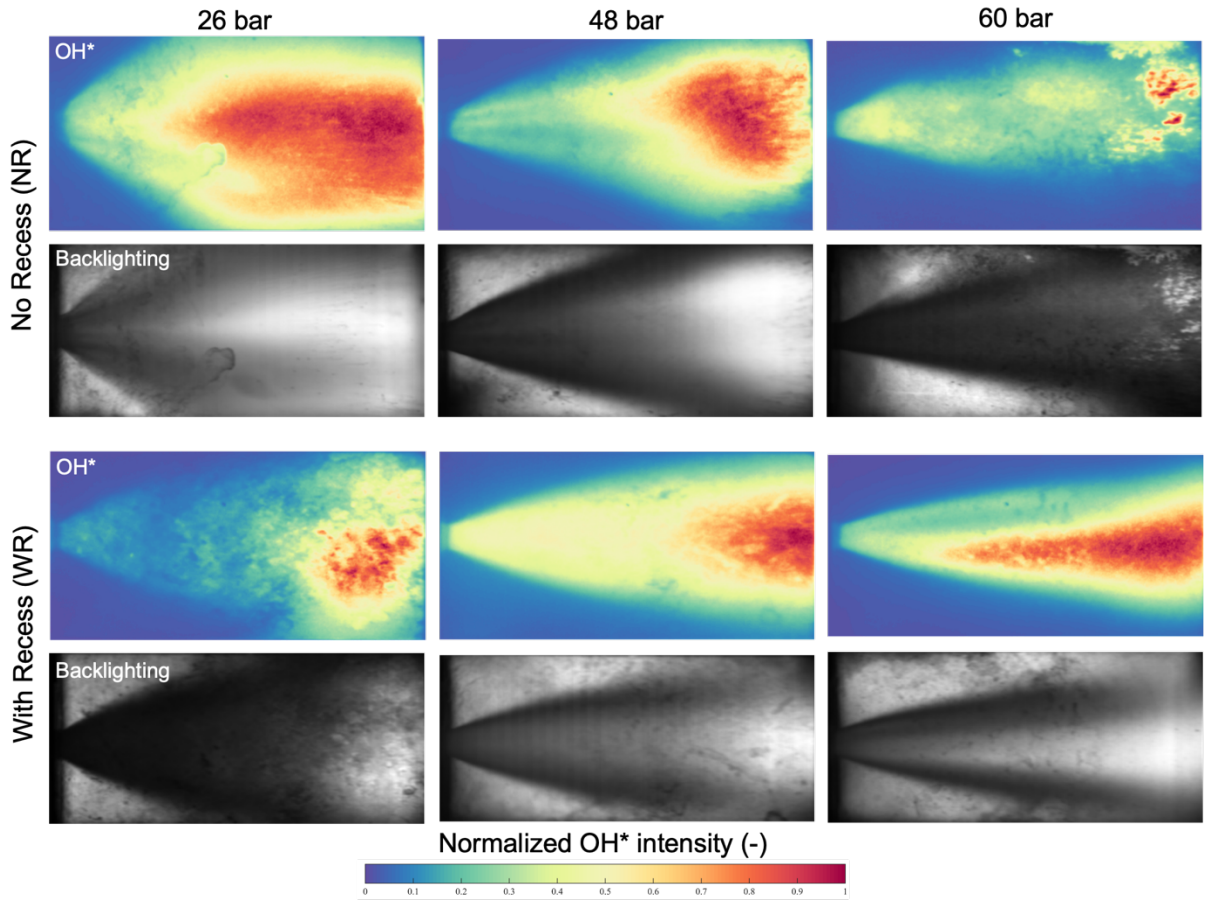

Figure 7. Time-averaged OH emission and backlighting images as a function of pressure, and with or without recess of the LOX post.*

4. OPERATING POINT DEPENDENCE

The flame structure and surface temperature measurements are analyzed separately according to the operating points in the following paragraphs.

4.1. Flame structure

Time-averaged images of OH* emission and backlighting are calculated for 35 s < t < 45 s from 10 000 instantaneous images thanks to the acquisition at 1 kHz frame rate for all six operating points. They are shown in Fig. 7. Time-averaged images of CH* emission are not shown here but present the same conic flame shape. As previously seen on instantaneous images (Fig. 6), OH* images show a common similarity: a brighter zone on the right part of the window downstream of the injection. The intensity is lower on the first two-thirds of the left part of the window, the flame emission being masked by the liquid jet. The darker zones on the backlighting images correspond with the darker zones of OH* images. Note that these images are spatially convoluted and show a 2D representation of the 3D flame. Besides, more light is accumulated along the line of sight as the diameter of these conic flames increases. Deposits on windows, mask the flame as seen at NRP26 operating point.

OH* time-averaged images show that the flame opening angle decreases with increasing chamber pressure with respect to the liquid jet opening angle. The flame seems slightly less open with the recessed injection element at constant pressure.

As observed in past studies in similar conditions [15, 21], an ice ring is observed time-to-time in the vicinity of the injection element. Fig. 8 shows an example of instantaneous OH* and backlighting close-ups with a significant ice ring formation. This ice may result from water condensation, recirculating around the flame, in contact with the cold injection plate, and the cryogenic methane injection. It expands over a few millimeters with a cylindrical shape and surrounds the liquid jets, and the flame anchoring is entirely masked. It has been observed that this ice ring grows, not necessarily in a symmetrical way, then breaks away and reappears again. Smaller or larger pieces of ice sometimes break off, significantly influencing the liquid jet and the flame dynamic and stability. Besides, darker narrow stripes are also identifiable on the backlighting image emerging from the ice ring and may result from melting ice. The same stripes are visible on the OH* image, locally reducing the light intensity passing through them. This effect is less visible in the time-averaged images that smooth out the phenomenon. The stripes are still well identifiable at NRP26 and

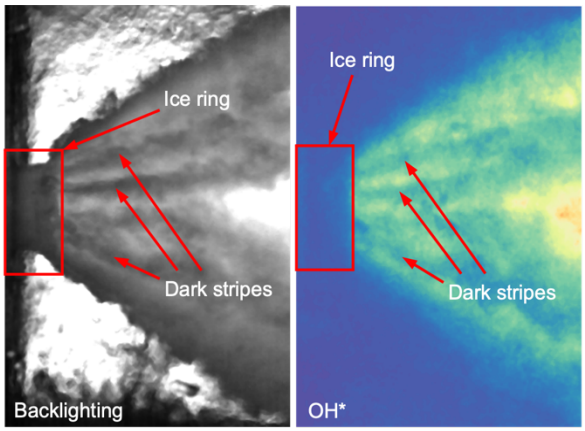

Figure 8. Evidence of an ice ring at the injection element exit at t = 44.65 s at NRP26 operating point. Instantaneous OH and backlighting images.*

NRP48 operating points. More than two flame fronts can thus appear when performing an Abel deconvolution because these stripes are at a lower intensity, so their interpretation must be made with caution [21].

Judging flame anchoring is challenging. Although all the flames studied seem anchored on the injection element and no intermittent flame detachments have been observed, the ice ring hides the injection element vicinity and, thus, the exact anchoring location. Moreover, it is impossible to say whether the flames are anchored with the recessed injection element.

4.2. Surface temperature

The surface temperatures in the 2nd visualization module at WRP48 operating point are shown in Fig. 9. LIP measurements on the blind window are in good agreement with the ones from the wall thermocouple. One critical phenomenon captured by LIP measurements is the temperature peak at t = 28.5 s due to a higher mixture ratio during the injection of gaseous methane. It is not well-captured and delayed by the wall thermocouple whose response time (~300-500 ms) is longer. LIP measurements may not give the proper temperature peak because of the acquisition at 10 Hz. Still, single-shot measurements allow detecting the temperature dynamics during a hot fire test, which would not be possible with LIP average signals. The wall thermocouple systematically underestimates the temperature peak after ignition for all operating points. The temperature peak due to ignition of the H_2/O_2 torch is even sometimes captured (see Fig. 10 and 11).

The internal temperature of the silica window (Mod. 2 int.) is very close to the one measured by K1 thermocouple. However, the temperature peak is lower on the window but delayed with the thermocouple, again due to a slower response time of a few tenths of a second. There is, however, no increase of the temperature in the external face of

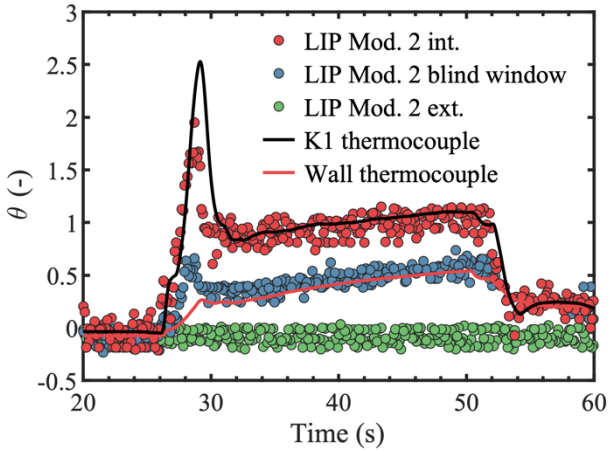

Figure 9. Temporal evolution of normalized surface temperatures in the 2nd visualization module at WRP48 operating point.

the silica window, whatever the operating point. This observation allows to model the silica window as a 1D semi-infinite medium. Fitting this model on the measurements allows the estimation of the local convection coefficient and the prediction of the temperature at any depth inside the walls. This is presented in detail in Lechner et al. [28], which shows as well that convection is the predominant heat transfer mode and fixes surface temperature downstream the flame.

Fig. 10 shows surface temperatures in the 1st and 2nd visualization modules at NRP48 operating point. The first difference comes from the increase of external face temperatures, so convection may not be the predominant phenomenon near the flame. The increase of temperature and the main temperature peaks are identical for the internal surfaces. After t = 32 s, the temperature still rises downstream of the flame, whereas it is constant and lower near the flame. The lower temperature of the dense phase observed recirculating around the flame would then result in a lower convection coefficient in the boundary of the internal LIP measurement and thus a lower surface temperature.

Dependence on chamber pressure and injection element geometry is highlighted in Fig. 11 for the internal surface temperature of the silica window in the 2nd module. Different pressure ramps were reached for the NRP26 operating point to investigate potential low-frequency instabilities. Mass flow rates of propellants were slightly adjusted during this process, thus modifying the mixture ratio and thus the gas temperature. Therefore, these slow oscillations in time should not be associated with the pressure value or the absence of LOX post recess. This phosphor thermometry setup associated with the FSF method showed the ability to track small power modulations [28]. A small temperature peak is also noticeable at the end of the run, around t = 55 s for the NRP26 operating point. It results from a short

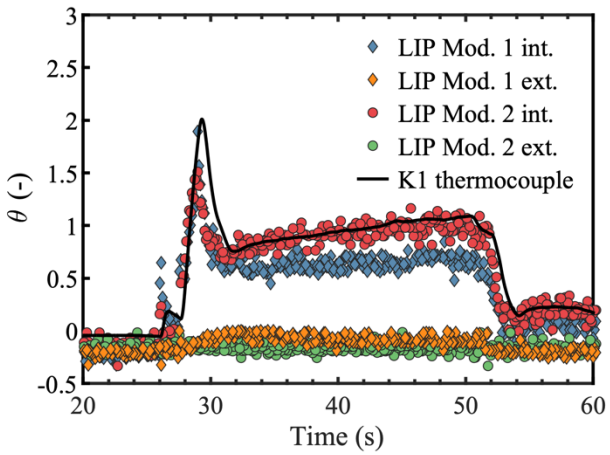

Figure 10. Temporal evolution of normalized internal and external surface temperatures of silica windows in the 1st and 2nd module at NRP48 operating point.

re-ignition of the flame, thereafter prevented with the nitrogen purge. Note that temperature measurements are a bit noisier for the WRP60 operating point due to a lower signal-to-noise ratio of the phosphorescence signal. Anyway, all six plots show globally the same characteristics: the broad temperature peak of LOX/GCH_4 flame ignition, again delayed with K1 thermocouple, followed by a continuous temperature rise from $\theta = 0.7$ up to $\theta = 1$ concluded by the decrease after the flame extinction. Still, some differences exist at 26 bar. Indeed, the temperature peak at ignition is broader and seems to include the smaller one from the torch ignition compared to 48 and 60 bar operating points for which the first peak is identifiable and separated from the principal. From a thermal point of view, recessing the LOX post shows little apparent effect.

It is, however, challenging to make any conclusions with respect to the operating points in the 1st module, near the flame. The surface temperature is more dependent on the behavior of the flame and the liquid jets. There are more fluctuations in time, the flame or the jets impacting time to time the bottom window.

5. CONCLUSIONS

LOX/LCH_4 cryogenic flames at typical rocket engine gas generator conditions: very low mixture ratio and high pressure, have been investigated thanks to various optical diagnostics implemented simultaneously on the BHP combustion chamber of the MASCOTTE test bench operated by ONERA.

Imaging the flame with both liquid, or transcritical, oxygen and methane was challenging, the flame being often partially masked by the dense jets. Deposits on windows, progressive along test duration, are another source of poor signal-to-noise ratio. Still, time-averaged images give satisfactory results to judge the operating conditions influence on the flame shape. The flame opening angle appears to decrease with the increase of chamber pressure and with the LOX post recess. An ice ring was identified at the flame foot, significantly affecting the flame behavior and hiding the flame anchoring. A dedicated camera in the visible domain will be implemented in a next campaign for further investigations.

Phosphor thermometry and the Full Spectrum Fitting post-processing method have proven to be particularly well adapted to track transient temporal temperature evolutions in these harsh conditions. In contrast to conventional sensors, single-shot LIP measurements allowed the clear identification of temperature peaks. Besides, measurements near and downstream of the flame showed different thermal transfer modes. These data are crucial information for more accurate numerical simulations. Near the flame, the surface temperature is lower, probably in a zone of recirculating water. Ice formation from the injection element exit and around the flame anchoring suggests a cold injection plate. This will be investigated in the next campaign thanks to additional LIP measurements.

Laser extinction was successfully implemented for the first time on this bench to obtain a dynamic estimation of soot production. However, quantitative results and judging the dependence on the operating conditions are challenging and need more investigation. Therefore, additional axial measurements will be implemented in the next campaign to identify the stage of soot formation. Soot particles were also sampled at each operating point. They will be soon analyzed by Transmission Electron Microscopy (TEM) to identify their type, morphology, and size, which are essential knowledge for the validation of the hypotheses assumed to determine the soot volume fraction. They are coupled with gas samples downstream of the flame [20], which analysis by gas chromatography will give valuable information in terms of soot precursors.

A following experimental test campaign will study the injection element design on the flame characteristics.

6. ACKNOWLEDGMENTS

This work is part of an ongoing joint Ph.D. between EM2C laboratory and ONERA, co-piloted by CNES and ArianeGroup. The authors would like to thank the members of the MASCOTTE test bench for their involvement during the campaign.

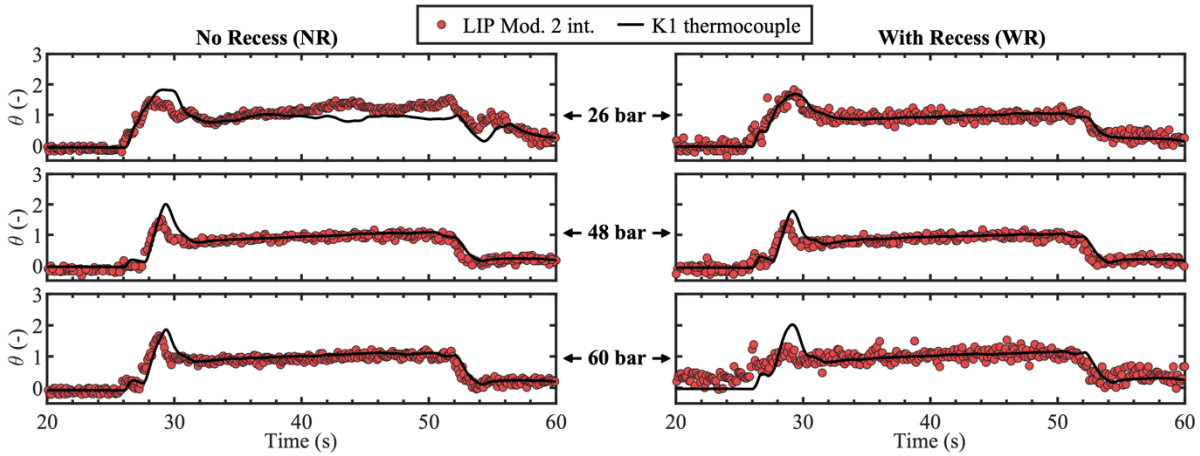

Figure 11. Temporal evolution of the normalized internal temperature in the 2nd module measured by LIP and by K1 thermocouple as a function of pressure, and with or without recess of the LOX post.

7. REFERENCES

1. Guiberti, T.F., Durox, D., Scouflaire, P. & Schuller, T. (2015). Impact of heat loss and hydrogen enrichment on the shape of confined swirling flames. *Proceedings of the Combustion Institute*. (35), 2, 1385–1392.

2. Mercier, R., Guiberti, T.F., Chatelier, A., Durox, D., Gicquel, O., Darabiha, N., Schuller, T., et al. (2016). Experimental and numerical investigation of the influence of thermal boundary conditions on premixed swirling flame stabilization. *Combustion and Flame*. (171), 42–58.

3. Ahn, K., Kim, J.-G. & Choi, H.-S. (2014). Effects of injector recess on heat flux in a combustion chamber with cooling channels. *Aerospace Science and Technology*. (37), 110–116.

4. Marshall, W.M., Pal, S., Woodward, R.D. & Santoro, R.J. (2005). Benchmark Wall Heat Flux Data for a GO2/GH2 Single Element Combustor. *41st AIAA/ASME/SAE/ASEE*.

5. Vingert, L., Grenard, P., Lévy, F., Nicole, A., Dorey, L.-H. & Benito, M.M. (2019). Heat Transfer Measurements in a Water-Cooled Rocket Combustion Chamber Operated with Oxygen/Methane Mixtures at the Mascotte Test Facility. *32nd ISTS & 9th NSAT Joint Symposium*.

6. Grenard, P., Fdida, N., Vingert, L., Dorey, L.-H., Selle, L. & Pichillou, J. (2019). Experimental investigation of heat transfer in a subscale liquid rocket engine at high mixture ratio. *Journal of Propulsion and Power*. (35), 3, 544–551.

7. Schoenman, L. (1991). LOX/propane and LOX/ethanol combustion chamber heat transfer. *Journal of Propulsion and Power*. (7), 4, 538–548.

8. Meland, L. & Thompson, F. (1989). History of the Titan liquid rocket engines. *25th Joint Propulsion Conference*.

9. Hernandez, R. & Mercer, S. (1987). Carbon deposition characteristics of LO2/HC propellants. *23rd Joint Propulsion Conference*.

10. Lausten, M., Rousar, D. & Buccella, S. (1985). Carbon deposition with LOX/RP-1 propellants. *21st Joint Propulsion Conference*.

11. Schmitt, T. (2020). Large-Eddy Simulations of the Mascotte Test Cases Operating at Supercritical Pressure. *Flow, Turbulence and Combustion*. (105), 159–189.

12. Kendrick, D., Herding, G., Scouflaire, P., Rolon, C. & Candel, S. (1999). Effects of a recess on cryogenic flame stabilization. *Combustion and Flame*. (118), 3, 327–339.

13. Tripathi, A., Juniper, M., Scouflaire, P., Rolon, J.-C., Durox, D. & Candel, S. (1999). LOx tube recess in cryogenic flames investigated using OH and H2O emission. *35th Joint Propulsion Conference and Exhibit*.

14. Lux, J. & Haidn, O. (2009). Effect of Recess in High-Pressure Liquid Oxygen/Methane Coaxial Injection and Combustion. *Journal of Propulsion and Power*. (25), 1, 24–32.

15. Theron, M., Martin Benito, M., Vieille, B., Vingert, L., Fdida, N., Mauriot, Y., Blouquin, R., et al. (2019). Experimental and numerical investigation of LOX/Methane Cryogenic Combustion at low mixture ratio. *EUCASS 2019*.

16. Vingert, L., Ordonneau, G., Fdida, N. & Grenard, P. (2016). A Rocket Engine under a Magnifying Glass. *AerospaceLab*. 15.

17. Brübach, J., Pflitsch, C., Dreizler, A. & Atakan, B. (2013). On surface temperature measurements with thermographic phosphors: A

review. *Progress in Energy and Combustion Science*. (39), 1, 37–60.

18. Lechner, V., Betrancourt, C., Mirat, C., Scouflaire, P. & Ducruix, S. (in revision). Full spectrum fitting method: a new approach for instantaneous phosphor thermometry in harsh environments. *Experiments in Fluids*.

19. Simonsson, J., Olofsson, N.-E., Török, S., Bengtsson, P.-E. & Bladh, H. (2015). Wavelength dependence of extinction in sooting flat premixed flames in the visible and near-infrared regimes. *Applied Physics B*. (119), 4, 657–667.

20. Vingert, L., Sicard, M., Fdida, N., Delhaye, D., Lechner, V. & Theron, M. (accepted). Experimental characterization of oxygen/methane combustion in rocket engine gas generator operating conditions, in a mono-injector combustor on the Mascotte facility. *EUCASS 2022*.

21. Singla, G., Scouflaire, P., Rolon, C. & Candel, S. (2005). Transcritical oxygen/transcritical or supercritical methane combustion. *Proceedings of the Combustion Institute*. (30), 2, 2921–2928.

22. Lux, J. & Haidn, O. (2009). Flame Stabilization in High-Pressure Liquid Oxygen/Methane Rocket Engine Combustion. *Journal of Propulsion and Power*. (25), 1, 15–23.

23. Habiballah, M., Orain, M., Grisch, F., Vingert, L. & Gicquel, P. (2006). Experimental Studies of High-Pressure Cryogenic Flames on the Mascotte Facility. *Combustion Science and Technology*. (178), 1–3, 101–128.

24. Liu, F. & Smallwood, G.J. (2010). Effect of aggregation on the absorption cross-section of fractal soot aggregates and its impact on LII modelling. *Journal of Quantitative Spectroscopy and Radiative Transfer*. (111), 2, 302–308.

25. Bladh, H., Johnsson, J., Olofsson, N.-E., Bohlin, A. & Bengtsson, P.-E. (2011). Optical soot characterization using two-color laser-induced incandescence (2C-LII) in the soot growth region of a premixed flat flame. *Proceedings of the Combustion Institute*. (33), 1, 641–648.

26. Zerbs, J., Geigle, K.P., Lammel, O., Hader, J., Stirn, R., Hadef, R. & Meier, W. (2009). The influence of wavelength in extinction measurements and beam steering in laser-induced incandescence measurements in sooting flames. *Applied Physics B*. (96), 4, 683–694.

27. Snyder, R., Herding, G., Rolon, J.-C. & Candel, S. (1997). Analysis of Flame Patterns in Cryogenic Propellant Combustion. *Combustion Science and Technology*. (124), 1–6, 331–370.

28. Lechner, V., Betrancourt, C., Scouflaire, P., Vingert, L. & Ducruix, S. (submitted). Dynamic characterization of wall temperature in LOX/CH4 rocket engine operating conditions using phosphor thermometry. *Proceedings of the Combustion Institute*.